

Probing the symmetry breaking of a light–matter system by an ancillary qubit

Shuai-Peng Wang,^{1,2} Alessandro Ridolfo,³ Tiefu Li,^{4,5,*} Salvatore Savasta,^{6,†} Franco Nori,^{7,8,9} Y. Nakamura,^{9,10} and J. Q. You^{2,‡}

¹*Quantum Physics and Quantum Information Division,
Beijing Computational Science Research Center, Beijing 100193, China*

²*Interdisciplinary Center of Quantum Information,
State Key Laboratory of Extreme Photonics and Instrumentation,
and Zhejiang Province Key Laboratory of Quantum Technology and Device,
School of Physics, Zhejiang University, Hangzhou 310027, China*

³*Dipartimento di Fisica e Astronomia, Università di Catania, 95123 Catania, Italy*

⁴*School of Integrated Circuits, and Frontier Science Center for
Quantum Information, Tsinghua University, Beijing 100084, China*

⁵*Beijing Academy of Quantum Information Sciences, Beijing 100193, China*

⁶*Dipartimento di Scienze Matematiche e Informatiche,
Scienze Fisiche e Scienze della Terra, Università di Messina, I-98166 Messina, Italy*

⁷*Theoretical Quantum Physics Laboratory, Cluster for Pioneering Research, RIKEN, Wako, Saitama 351-0198, Japan*

⁸*Physics Department, The University of Michigan, Ann Arbor, Michigan 48109-1040, USA*

⁹*RIKEN Center for Quantum Computing (RQC), Wako, Saitama 351-0198, Japan.*

¹⁰*Department of Applied Physics, Graduate School of Engineering,
The University of Tokyo, Bunkyo-ku, Tokyo 113-8656, Japan*

Hybrid quantum systems in the ultrastrong, and even more in the deep-strong, coupling regimes can exhibit exotic physical phenomena and promise new applications in quantum technologies. In these nonperturbative regimes, a qubit–resonator system has an entangled quantum vacuum with a nonzero average photon number in the resonator, where the photons are virtual and cannot be directly detected. The vacuum field, however, is able to induce the symmetry breaking of a dispersively coupled probe qubit. We experimentally observe the parity symmetry breaking of an ancillary Xmon artificial atom induced by the field of a lumped-element superconducting resonator deep-strongly coupled with a flux qubit. This result opens a way to experimentally explore the novel quantum-vacuum effects emerging in the deep-strong coupling regime.

Introduction

Superconducting quantum circuits based on Josephson junctions (JJs) [1–8] have developed rapidly in recent years and demonstrated quantum advantage, over classical counterparts, in information processing [9, 10]. Now they are considered to be one of the most promising experimentally-realizable systems for quantum computing [11–13]. Also, the experimental advancements in superconducting qubit–resonator systems have stimulated theoretical and experimental researches on quantum optics in the microwave regime [14, 15]. As a solid-state version of cavity quantum electrodynamics (QED) [16, 17], circuit QED [18–20] has greater flexibility and tunability, and it can achieve ultrastrong and even deep-strong light–matter couplings to individual qubits [21–27], owing to the large dipole moment of the superconducting qubit (i.e., artificial atom) and the small mode volume of the resonator. When the qubit–resonator coupling approaches the nonperturbative ultrastrong regime, novel quantum-optics phenomena occur [28–33], including puzzling modifications of the quantum vacuum of the system [34–40].

In the nonperturbative ultrastrong-coupling regime, the qubit–resonator system can be described by a quantum Rabi model. It is particularly interesting to harness controllable physical parameters to tune the quan-

tum vacuum of the system, since it becomes a novel entangled ground state $|G\rangle$ rather than the trivial product ground state of the Jaynes-Cummings model. In such an exotic quantum vacuum, while the average photon number in the resonator is nonzero, i.e., $\langle G|a^\dagger a|G\rangle \neq 0$, where $a^\dagger(a)$ is the creation (annihilation) operator of the resonator mode, the ground-state photons are actually virtual (tightly bound to the artificial atom [41]) and cannot be directly detected. Theoretically, it was proposed to employ non-adiabatic modulations [37], sudden turn-off of the qubit–resonator interaction [38], or a spontaneous decay mechanism of multi-level systems [39] to convert these virtual photons into real ones (similar to the dynamical Casimir effect [42, 43]), so as to generate radiation out of the resonator. However, these are still experimentally challenging.

In the standard model of particle physics, the W^\pm and Z weak gauge bosons obtain mass via the Higgs mechanism, in which the electroweak gauge symmetry $SU(2) \times U(1)$ is broken due to the interaction with a symmetry-broken vacuum field (the Higgs field) displaying a nonzero vacuum expectation value. In our experiment, we observe the parity symmetry breaking of a probe superconducting circuit (Xmon) dispersively coupled to a qubit–resonator system in the deep-strong coupling regime. This effect, although rather different (in

our case the broken symmetry is discrete and it is not spontaneous), shares some interesting analogies with the Higgs mechanism. At the optimal point, both the flux qubit and the qubit-resonator system have a well-defined parity symmetry [44]. In this parity-symmetry case, the quantum-vacuum expectation value of the resonator field is zero, $\langle G|(a + a^\dagger)|G\rangle = 0$, where $|G\rangle$ is the qubit-resonator ground state. With the external flux tuned away from the optimal point, parity-symmetry breaking is induced in the flux qubit and, in the presence of a very strong qubit-resonator coupling, it also significantly affects the resonator vacuum, giving rise to $\langle G|(a + a^\dagger)|G\rangle \neq 0$ [35]. In our experiment, the achieved qubit-resonator system is in the deep-strong coupling regime, so the quantum-vacuum state is very different and, when away from the optimal point, this can produce a sizable nonzero value of $\langle G|(a + a^\dagger)|G\rangle$ as well as observable symmetry breaking effects. Indeed, as demonstrated in our experiment, the qubit-resonator system is able to break the parity selection rule of the Xmon dispersively coupled to the resonator, thus enabling forbidden transitions. We should emphasize that the similarity between the Higgs mechanism and our observation only comes from two key features: (i) the symmetry-broken vacuum has a nonzero expectation value, and (ii) the field with a nonzero expectation value can induce symmetry breaking in another quantum system, in the absence of real excitations of the field. Of course, a system composed by just two qubits and a lumped-element resonator cannot fully reproduce the far more complex Higgs model.

Results

Deep-strongly coupled qubit-resonator circuit

The system is composed of a five-junction flux qubit deep-strongly coupled to a superconducting lumped-element resonator via a common Josephson junction (JJ) (Fig. 1). In addition, we use an Xmon as a quantum detector, which is capacitively coupled to the lumped-element resonator on the left and to a coplanar-waveguide resonator on the right. The whole device is placed in a dilution refrigerator cooled down to a temperature of ~ 30 mK.

Similar to the three-junction flux qubit [2], the five-junction flux qubit has both clockwise and counterclockwise persistent-current states. Away from the optimal point $\Phi_{\text{ext}} = (n + \frac{1}{2})\Phi_0$, where Φ_{ext} is the external flux threading the loop of the flux qubit, $\Phi_0 = h/2e$ is the superconducting flux quantum, and n is an integer, these two persistent-current states have an energy difference $\varepsilon = 2I_p\delta\Phi_{\text{ext}}$, depending on the maximum persistent current I_p and the flux bias $\delta\Phi_{\text{ext}} \equiv \Phi_{\text{ext}} - (n + \frac{1}{2})\Phi_0$. Also, there is a barrier between these two persistent-current states, which removes their degeneracy at the optimal point by opening an energy gap Δ . In the basis of eigenstates, the Hamiltonian of the flux qubit can be written as (setting $\hbar = 1$) $H_q = \omega_q\sigma_z/2$, where $\omega_q = \sqrt{\Delta^2 + \varepsilon^2}$ is

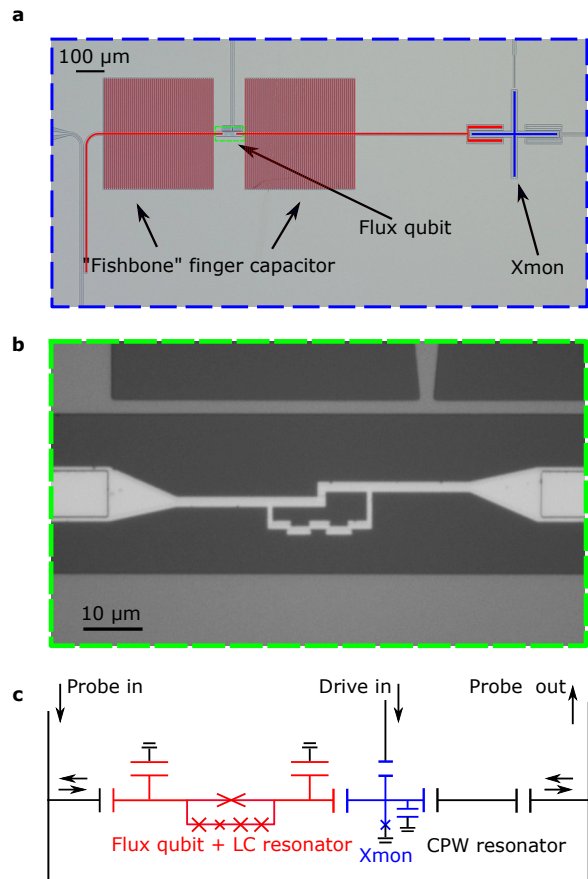


FIG. 1. **Device.** **a**, Optical image of the device. The lumped-element resonator is composed of two identical large “fishbone” interdigitated capacitors and a center conductor in between. The flux qubit consists of three identical larger JJs and a smaller JJ reduced by a factor of 0.42 in area. To enhance the coupling between the flux qubit and the lumped-element resonator, an even larger JJ (with its area doubled) is added in the qubit loop and shared with the center conductor. Extending to the left (right) is another section of $50\ \Omega$ coplanar waveguide which couples to the input signal line (the Xmon qubit). **b**, Zoom-in optical image of the area denoted by the green rectangular box in **a**. **c**, Circuit diagram of the device (cf. Supplementary Fig. 1).

the transition frequency of the qubit and σ_z is a Pauli operator. The quantum two-level system is a good model for the flux qubit because of its relatively large anharmonicity.

Compared to the coplanar-waveguide resonator, the lumped-element resonator has the advantage of only a single resonator mode [24]: $H_r = \omega_r a^\dagger a$, where ω_r is the resonance frequency of the resonator mode. This ω_r is V-shaped versus $\delta\Phi_{\text{ext}}$ around the optimal point [24] because the inductance across the qubit loop, as part of the total inductance of the lumped-element resonator, depends approximately linearly on $|\delta\Phi_{\text{ext}}|$. The large JJ shared by the flux qubit and the lumped-element resonator acts as an effective inductance to produce an inter-

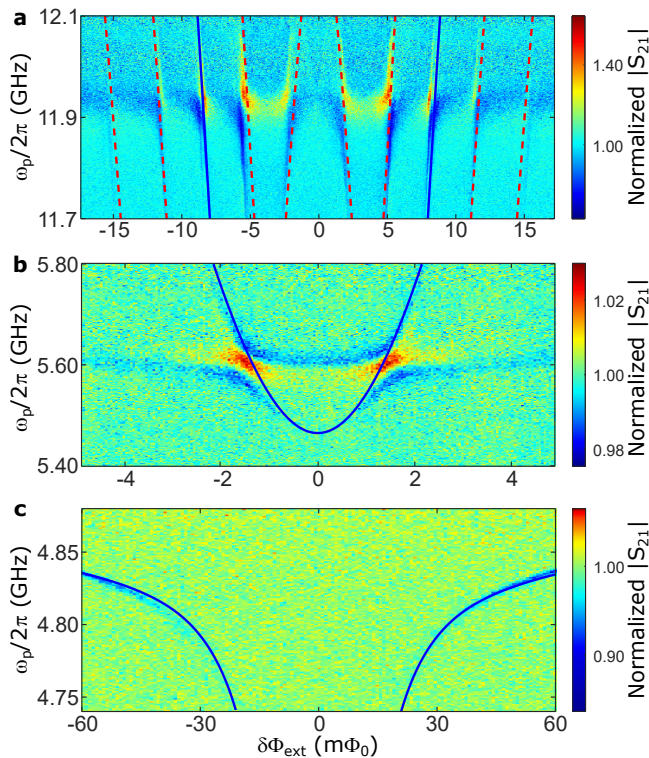


FIG. 2. **Reflection spectra.** Reflection spectra of the deep-strongly coupled qubit-resonator system versus the external flux bias $\delta\Phi_{\text{ext}}$ and the probe frequency ω_p around $\Phi_{\text{ext}} = (3 + \frac{1}{2})\Phi_0$ (which is a more stable flux bias point than $\Phi_{\text{ext}} = \frac{1}{2}\Phi_0$ in our system). The solid blue curves in **a-c** are the fitted transition frequencies between the ground state to the third-, second- and first-excited states of the qubit-resonator system, respectively (i.e., ω_{03} , ω_{02} , and ω_{01}). In **a**, the additional transitions indicated by the dashed red curves correspond to sideband transitions (assisted by the Xmon levels) in the system. Source data are provided as a Source Data file.

action between them, $H_{\text{int}} = g[\cos\theta\sigma_z - \sin\theta\sigma_x](a^\dagger + a)$, where $\tan\theta = \Delta/\varepsilon$, and $g = MI_p I_r$ is the coupling strength, with $M \approx L_c$ being the mutual inductance and $I_r = \sqrt{\omega_r/2(L_0 + L_c)}$ the vacuum fluctuation current along the center conductor of the lumped-element resonator, where L_c is the inductance of the large JJ and L_0 is the geometry inductance. When the qubit-resonator coupling is in the ultrastrong or deep-strong regime, one cannot apply the rotating-wave approximation (RWA) to H_{int} , and the Hamiltonian of the qubit-resonator system is written as

$$H_s = \frac{1}{2}\omega_q\sigma_z + \omega_r a^\dagger a + g[\cos\theta\sigma_z - \sin\theta\sigma_x](a^\dagger + a), \quad (1)$$

i.e., the generalized quantum Rabi model [15].

We can extract the parameters in H_s by fitting the reflection spectra of the qubit-resonator system, as measured by applying a probe tone to the system. Around $\omega_p/2\pi = 4.8$ GHz (near the bare frequency of the lumped-

element resonator) and 5.6 GHz, clear transitions are observed; of which the corresponding frequencies are found to be consistent with the transition frequencies from the ground state $|G\rangle \equiv |0\rangle_s$ to the first- and second-excited states, $|1\rangle_s$ and $|2\rangle_s$ of the qubit-resonator system, respectively, i.e., ω_{01} and ω_{02} (see the solid fitting curves in Figs. 2c and 2b). Around $\omega_p/2\pi = 11.9$ GHz, we observe the transition from the ground state $|G\rangle$ to the third-excited state $|3\rangle_s$ (Fig. 2a), with the solid fitting curves corresponding to ω_{03} . Moreover, similar to those in Ref. 26, additional transitions are observed in Fig. 2a, which are attributed to the sideband transitions (the dashed curves in Fig. 2a) involving the Xmon levels as well, see Supplementary Information.

Near 5.6 GHz and 11.9 GHz, the transmission background of the probe tone changes abruptly, forming two band edges (see Supplementary Fig. 2). The qubit-resonator system coupled to the band edges in Figs. 2a and 2b is analogous to the case of an atom coupled to a band edge in a photonic crystal waveguide [45, 46]. The abrupt changes in the transmission background originate from the wire bonding and filters. Near the band edge, a photon emitted by the atom (in our case it is the qubit-resonator system) is Bragg reflected and reabsorbed, resulting in the emergence of spectrally resolvable polariton states (similar to the vacuum Rabi splitting), which will disappear away from the band edge [45].

By fitting the transition frequencies ω_{01} , ω_{02} and ω_{03} with experimental results in Fig. 2, we can derive the parameters of the generalized Rabi model in Eq. (1), which are $I_p = 245$ nA and $\Delta/2\pi = 15.0$ GHz for the flux qubit, $\omega_r/2\pi = 4.82$ GHz for the lumped-element resonator, and $g/2\pi = 4.55$ GHz for the qubit-resonator coupling. Here the obtained resonance frequency $\omega_r/2\pi = 4.82$ GHz is the value when the external flux bias is at the optimal point $\delta\Phi_{\text{ext}} = 0$. In our qubit-resonator system, we achieve $g/\omega_r \approx 0.944$, indicating that it indeed reaches the deep-strong coupling regime $g/\omega_r \sim 1$.

When $\delta\Phi_{\text{ext}} = 0$ ($\theta = \pi/2$), the deep-strongly coupled system in Eq. (1) reduces to the standard quantum Rabi model. Instead of a trivial (product) ground state $|g, 0\rangle$ in the Jaynes-Cummings model, it has a quantum vacuum (i.e., entangled ground state) $|G\rangle$, with $\langle G|a^\dagger a|G\rangle \neq 0$. This standard Rabi model has a well-defined parity symmetry, characterized by $\sigma_z e^{i\pi a^\dagger a}$, which ensures that the ground state is a superposition of all states with an even number of excitations [28]. For this quantum vacuum, $\langle G|(a + a^\dagger)|G\rangle = 0$. When $\delta\Phi_{\text{ext}} \neq 0$, H_s in Eq. (1) has an extra longitudinal coupling term proportional to σ_z . It breaks the parity symmetry of the model, and hence both even and odd numbers of excitations are allowed in the new ground state [35] as well as in the excited states of the coupled system. Now, both $\langle G|a^\dagger a|G\rangle \neq 0$ and $\langle G|(a + a^\dagger)|G\rangle \neq 0$.

Detection of the induced symmetry breaking

Below we harness an Xmon [7] to detect the symmetry breaking of the lumped-element resonator. The Xmon is both largely detuned and weakly coupled to it via a small capacitor (cf. Fig. 1a). In such a dispersive regime, the effect of the Xmon on the qubit–resonator system is greatly reduced. The Xmon can be modeled by the Hamiltonian $H_X = 4E_c n^2 - E_J \cos \varphi$, where E_c is the single-electron charging energy of the JJ, E_J is the Josephson coupling energy, $n = -i\partial/\partial\varphi$, and φ is the phase drop across the JJ. In the Xmon, the metallic cross and the ground metal provides the JJ with a large shunt capacitor to reduce its sensitivity to the charge noise [5, 6].

The Xmon’s parameters can be determined with the dispersive readout technique by coupling the Xmon to a coplanar-waveguide resonator (see Fig. 1c and Supplementary Fig. 1). The resonance frequency of this waveguide resonator is measured to be $\omega_{\text{CPW}}/2\pi = 3.554$ GHz and the coupling strength between the waveguide resonator and the Xmon qubit is $g_X/2\pi = 28$ MHz. Then, we obtain the transition frequency $\omega_X/2\pi = 5.181$ GHz of the Xmon qubit and its anharmonicity $A/2\pi = -0.16$ GHz. With these parameters as well as the relations $\omega_X = \sqrt{8E_c E_J} - E_c$ and $A = -E_c$, we have $E_c/2\pi = 0.16$ GHz and $E_J/2\pi = 20.97$ GHz. Because the lumped-element resonator couples to the Xmon, it induces an offset charge to the Josephson junction, leading H_X to $\tilde{H}_X = 4E_c(n - n_R)^2 - E_J \cos \varphi$, where $n_R = i\frac{g'}{8E_c}(a - a^\dagger)$, and $g' \approx g_X$ (by a symmetric design) is the coupling strength between the lumped-element resonator and the Xmon qubit.

The total Hamiltonian of the deep-strongly coupled qubit–resonator system plus the Xmon can be expressed as $H_{\text{tot}} = H_s + \tilde{H}_X$. Owing to the large transition frequency between the ground and first-excited states, the deep-strongly coupled qubit–resonator system nearly stays in the ground state $|G\rangle$ at the temperature ~ 30 mK.

Note that in the dispersive regime, where the Xmon–resonator coupling rate is much lower than the corresponding detuning, the energy transitions of the Xmon are almost unaffected by the interaction (i.e., flux-bias-insensitive) and can be easily identified with standard spectroscopic techniques. We also observe that, neglecting the interaction between the resonator and the flux qubit, or considering a flux qubit at the optimal point, the Xmon–resonator system displays parity symmetry. On the contrary, when the qubit is brought out of the optimal point, the very strong qubit–resonator coupling strength can induce a symmetry breaking of the Xmon, even for moderate Xmon–resonator coupling strengths (see Supplementary Information).

In Figs. 3a and 3b, we show the single- and two-photon transitions between the lowest two levels of the Xmon using two-tone spectroscopy. Here the resonance frequency of the single-photon transition corresponds to the transition frequency ω_X of the Xmon qubit, and the resonance

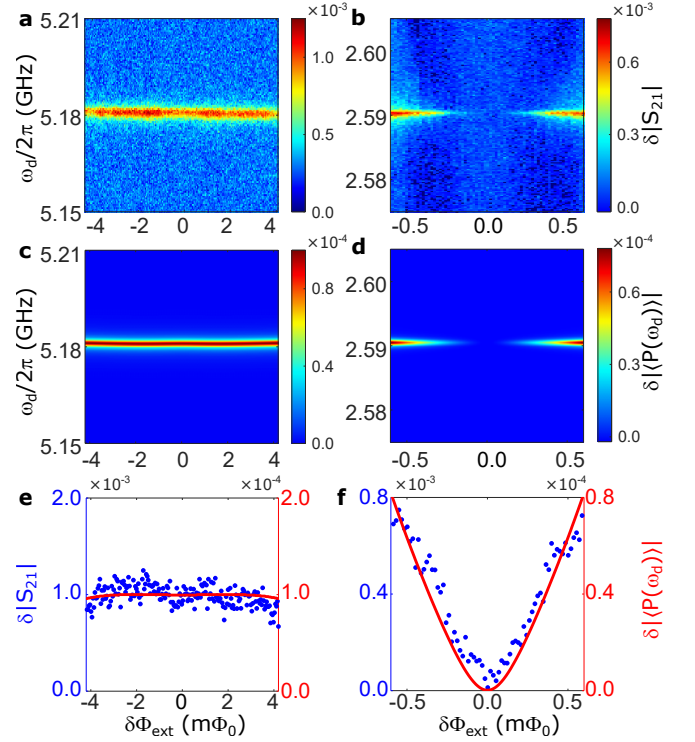


FIG. 3. **Excitation spectra.** Excitation spectra of the Xmon qubit versus the external flux bias $\delta\Phi_{\text{ext}}$ and the drive frequency ω_d around $\Phi_{\text{ext}} = (3 + \frac{1}{2})\Phi_0$. The frequency of the probe tone is fixed at 3.554 GHz, in resonance with the $\lambda/2$ mode of the coplanar-waveguide resonator. **a** and **b** show the experimental results, corresponding to the single- and two-photon transitions of the Xmon qubit with frequencies ω_X and $\frac{1}{2}\omega_X$, respectively. **c** and **d** show the simulated results. The theoretical calculations display the changes in the amplitude of the Xmon polarization $|\langle P(\omega_d) \rangle|$. Loss rates for the flux qubit, lumped-element resonator and Xmon are chosen to be $\gamma^{(q)}/2\pi = \gamma^{(a)}/2\pi = \gamma^{(b)}/2\pi = 2$ MHz, for simplicity and to be consistent with the observed linewidth in **a**. **e** (**f**), Cross sections along the excitation spectra in **a** (**b**) and **c** (**d**) when $\omega_d/2\pi = 5.181$ GHz (2.5905 GHz). Source data are provided as a Source Data file.

frequency of the two-photon transition is $\frac{1}{2}\omega_X$. In our chip, $\frac{1}{2}\omega_X$ is designed to be well separated from both ω_{01} and $\frac{1}{2}\omega_{02}$ of the deep-strongly coupled qubit–resonator system to avoid any unwanted transitions. The drive power (-65 dBm) applied at the local drive port for exciting the two-photon transition is much stronger than that for the single-photon transition (-120 dBm). In Fig. 3b, the signal of the two-photon transition is found to disappear at the optimal point $\delta\Phi_{\text{ext}} = 0$, evidencing that the well-defined parity symmetry of the standard Rabi model preserves the parity selection rule of the Xmon. When deviating from the optimal point, the parity-symmetry breaking in H_s , in addition to producing a nonzero vacuum expectation value $v = \langle G|(a + a^\dagger)|G\rangle \neq 0$, is able to break the parity symmetry of the Xmon artificial atom, without however inducing any $\delta\Phi_{\text{ext}}$ dependent Lamb

shift. Figure 3b shows that even a very small deviation from the parity symmetry point of the system Hamiltonian, which can be quantified by the adimensional parameter $\cot\theta = \varepsilon/\Delta \simeq 10^{-2}$, is able to activate two-photon transitions in the Xmon, in agreement with the theoretical calculations in Fig. 3d.

These results can be described by adopting a simplified model for the Xmon using only its four lowest energy levels. Considering the large detunings ($\gtrsim 20$ GHz), the effects from higher levels are negligible. With the Xmon now approximated as a four-level system (qudit), the total Hamiltonian of the qubit-resonator system plus the Xmon can be written as

$$H_{\text{tot}} = H_s + H_X^{(4)} - g'(a - a^\dagger)(b - b^\dagger), \quad (2)$$

where $b = \sum_{n=0}^3 \sqrt{n+1} |n\rangle\langle n+1|$ is the annihilation operator for the Xmon, and $H_X^{(4)} = \sum_{n=0}^3 \varepsilon_n |n\rangle\langle n|$ is the bare Xmon energy (H_X), projected into the reduced four-dimensional Hilbert space. We can evaluate the single- and two-photon absorptions under coherent drive of the Xmon by studying its effective polarization $\langle P(\omega_d) \rangle = \text{Tr}[-i(b - b^\dagger)\rho(\omega_d)]$, with ρ being the density operator of the system. The latter can be calculated using the master equation approach in the dressed picture [47] (see Supplementary Information). The simulated results are shown in Figs. 3c and 3d, which are in a good agreement with the experimental observations. This demonstrates the symmetry breaking of a quantum system which is coupled to the vacuum of another quantum system displaying symmetry breaking. Note that the deep-strongly coupled qubit-resonator system nearly stays in the ground state $|G\rangle$ at a temperature of ~ 30 mK, and in the present case of dispersive coupling with a largely detuned Xmon. Moreover, no real excitations of this system are coherently generated by the coherent drive at $\omega_d \simeq \omega_X/2$. We also point out that here the symmetry breaking is not spontaneous but due to the parity symmetry breaking of H_s in Eq. (2), induced by the presence of a flux offset applied to the flux qubit. However, the adimensional parameter ε/Δ , quantifying the degree of symmetry breaking induced by the flux offset on the flux qubit, is very small ($\varepsilon/\Delta \simeq 10^{-2}$) at $\delta\Phi_{\text{ext}} = 0.1$ m Φ_0 , when the Xmon two-photon transitions start to be observed (see Fig. 3b) and it does not affect the transition frequency of the Xmon. According to the additional calculations shown in Supplementary Fig. 6, the two-photon signals of the Xmon disappear if the effective coupling g/ω_r between the flux qubit and the LC resonator is reduced to 0.6. This provides evidence that the observed induced symmetry breaking of the Xmon is a unique feature in the near deep-strong coupling regime.

We observe that the interaction-induced symmetry breaking mechanism detected here is more complex with respect to the Higgs mechanism and to that described

in Ref. 35. In these two cases, the effect is directly induced by the vacuum expectation value of the field. For example, for $w = \langle G|(a - a^\dagger)|G\rangle \neq 0$, the Xmon-resonator interaction in Eq. (2) could be approximated as $\sim -g'w(b - b^\dagger)$. It can be shown that this term directly determines the symmetry breaking of the probe qubit in Ref. 35. However, in the present case, it turns out that $w = 0$, since the inductive coupling between the resonator and the flux qubit determines $w = 0$ and $v \neq 0$. Nonetheless, a full quantum analysis (see Supplementary Information) shows that in such a case ($w = 0$) as well, the Xmon can undergo symmetry breaking, when interacting with a field with no real excitations and displaying symmetry breaking. Using a probe qubit which is inductively coupled to the resonator would give rise to a symmetry breaking mechanism directly determined by the nonzero vacuum expectation value $v = \langle G|(a + a^\dagger)|G\rangle \neq 0$. In the present case, the symmetry breaking of the qubit-resonator system determines a nonzero matrix element entering the Xmon two-photon transition rate; thus enabling two-photon transitions in the Xmon. Considering the eigenstates of the total Hamiltonian H_{tot} , the two-photon transition rate is proportional to the product $|Y_{0,1}Y_{1,2}|$, where $Y_{i,j} = \langle E_i | -i(b - b^\dagger) | E_j \rangle$, with $|E_j\rangle$ eigenvectors of H_{tot} sorted from the lower to the higher corresponding energy levels. Thus, with $|E_0\rangle$ being the ground state of the whole interacting system, we identify $|E_1\rangle$ as the first excited level of H_s (slightly dressed by the interaction with the Xmon) and $|E_2\rangle$ the corresponding first excited dressed level of $H_X^{(4)}$. It turns out that $Y_{0,1}$ as well as $Y_{0,2}$ are nonzero and almost constant in the interval of flux offset reported here, while $Y_{1,2}$ is very well approximated by a linear function of $\delta\Phi_{\text{ext}}$ (see Supplementary Fig. 4) and it is zero for $\delta\Phi_{\text{ext}} = 0$, due to the parity symmetry. This explains the onset of the parity-symmetry breaking felt by the Xmon.

Discussion

One interesting future possibility is that the current experimental method could be used to characterise the spontaneous vacuum symmetry breaking in the Dicke model (i.e., equilibrium superradiant phase transition) when more flux qubits are integrated in the lumped-element resonator and operated at the optimal point simultaneously. If an equilibrium superradiant phase transition occurs, the small gap in the two-photon spectra of the Xmon in Fig. 3b will disappear; which means that two-photon transitions could be observed even for $\varepsilon/\Delta \simeq 0$. Note that in the present case, with a resonator interacting very strongly with only one flux qubit, we observe these parity-forbidden transitions for values $\varepsilon/\Delta \ll 1$ (specifically $\varepsilon/\Delta \gtrsim 0.01$). We also point out that, considering a setup with the capacitively coupled Xmon replaced by a galvanically coupled artificial atom (e.g. a flux qubit), the measured rate of parity-forbidden one- or two-photon transitions, would provide

a direct measurement of the vacuum field expectation value $\langle G|(a + a^\dagger)|G\rangle$, with a rate proportional to its square modulus [35].

In conclusion, we have experimentally probed the symmetry breaking of a lumped-element resonator, by observing the activation of two-photon transitions in a probe artificial atom (Xmon). The latter is dispersively coupled to the resonator and probed in the absence of any real coherent excitation of the resonator field; which however displays a nonzero vacuum expectation value, as confirmed by theoretical calculations. The violation of the Xmon parity selection rule comes from virtual paths enabled by its interaction with an electromagnetic resonator whose parity symmetry is significantly broken by the deep-strong light-matter interaction with a flux qubit. The experimental results are in very good agreement with our theoretical analysis. The proposed setting offers a novel way to explore quantum-vacuum effects emerging in the light-matter ultra-strong and deep-strong coupling regimes and can be used as a tool to explore the coherence properties of quantum vacua in these exotic hybrid quantum systems [48–50], and the occurrence of superradiant phase transitions in Dicke-like systems [36].

Methods

The experimental setup is shown in Supplementary Fig. 1. The superconducting lumped-element and coplanar-waveguide resonators are fabricated by patterning a niobium thin film of thickness 50 nm deposited on a 10×3 mm² silicon chip via electron beam lithography. The flux qubit is also fabricated on the silicon substrate in the middle of the center conductor of the lumped-element resonator by using both electron beam lithography and double-angle evaporation of aluminium. An external magnetic field generated by a magnetic coil surrounding the device is applied to tune the magnetic flux threading through the qubit loop. The Josephson junction in the Xmon is connected to the cross-shaped capacitor at one end and fabricated using separate steps of electron beam lithography and double-angle evaporation. Reflection spectra of the deep-strongly coupled qubit-resonator system at the frequency ω_p of the probe tone are measured with a vector network analyser (VNA). Another microwave signal at frequency ω_d is further applied at the local drive port of the Xmon for two-tone spectroscopy measurements. The input signals are attenuated and filtered at various temperature stages before finally reaching the sample. Also, two isolators and a low-pass filter (LPF) are used to protect the sample from the amplifier’s noise.

Data availability

The data that support the findings of this study are available from the corresponding authors upon reasonable request. Source data are provided with this paper.

Code availability

The code that support the findings of this study are available from the corresponding authors upon reasonable request.

* litf@tsinghua.edu.cn

† salvatore.savasta@unime.it

‡ jqyou@zju.edu.cn

- [1] Y. Nakamura, Y. A. Pashkin, and J. S. Tsai, Coherent control of macroscopic quantum states in a single-Cooper-pair box, *Nature* **398**, 786 (1999).
- [2] J. E. Mooij, T. P. Orlando, L. Levitov, L. Tian, C. H. van der Wal, and S. Lloyd, Josephson persistent-current qubit, *Science* **285**, 1036 (1999).
- [3] Y. Yu, S. Han, X. Chu, S. I. Chu, and Z. Wang, Coherent temporal oscillations of macroscopic quantum states in a Josephson junction, *Science* **296**, 889 (2002).
- [4] J. M. Martinis, S. Nam, J. Aumentado, and C. Urbina, Rabi Oscillations in a Large Josephson-Junction Qubit, *Phys. Rev. Lett.* **89**, 117901 (2002).
- [5] J. Q. You, X. Hu, S. Ashhab, and F. Nori, Low-decoherence flux qubit, *Phys. Rev. B* **75**, 140515(R) (2007).
- [6] J. Koch, T. M. Yu, J. Gambetta, A. A. Houck, D. I. Schuster, J. Majer, A. Blais, M. H. Devoret, S. M. Girvin, and R. J. Schoelkopf, Charge-insensitive qubit design derived from the Cooper pair box, *Phys. Rev. A* **76**, 042319 (2007).
- [7] R. Barends, J. Kelly, A. Megrant, D. Sank, E. Jeffrey, Y. Chen, Y. Yin, B. Chiaro, J. Mutus, C. Neill, P. O’Malley, P. Roushan, J. Wenner, T. C. White, A. N. Cleland, and J. M. Martinis, Coherent Josephson Qubit Suitable for Scalable Quantum Integrated Circuits, *Phys. Rev. Lett.* **111**, 080502 (2013).
- [8] F. Yan, S. Gustavsson, A. Kamal, J. Birenbaum, A. P. Sears, D. Hover, T. J. Gudmundsen, D. Rosenberg, G. Samach, S. Weber, J. L. Yoder, T. P. Orlando, J. Clarke, A. J. Kerman, and W. D. Oliver, The flux qubit revisited to enhance coherence and reproducibility, *Nat. Commun.* **7**, 12964 (2016).
- [9] F. Arute *et al.*, Quantum supremacy using a programmable superconducting processor, *Nature* **574**, 505 (2019).
- [10] Yulin Wu *et al.*, Strong Quantum Computational Advantage Using a Superconducting Quantum Processor, *Phys. Rev. Lett.* **127**, 180501 (2021).
- [11] G. Wendin, Quantum information processing with superconducting circuits: A review, *Rep. Prog. Phys.* **80**, 106001 (2017).
- [12] M. Kjaergaard, Mollie E. Schwartz, J. Braumüller, P. Krantz, J. I.-J. Wang, S. Gustavsson, and W. D. Oliver, Superconducting Qubits: Current State of Play, *Annu. Rev. Condens. Matter Phys.* **11**, 369 (2020).
- [13] S. Kwon, A. Tomonaga, G. L. Bhai, S. J. Devitt, and J. S. Tsai, Gate-based superconducting quantum computing, *J. Appl. Phys.* **129**, 041102 (2021).
- [14] J. Q. You and F. Nori, Atomic physics and quantum optics using superconducting circuits, *Nature* **474**, 589 (2011).
- [15] X. Gu, A. F. Kockum, A. Miranowicz, Y.-X. Liu, and F.

- Nori, Microwave photonics with superconducting quantum circuits, *Phys. Rep.* **718**, 1 (2017).
- [16] H. Mabuchi, and A.C. Doherty, Cavity quantum electrodynamics: coherence in context, *Science* **298**, 1372 (2002).
- [17] J.-M. Raimond, M. Brune, and S. Haroche, Manipulating quantum entanglement with atoms and photons in a cavity, *Rev. Mod. Phys.* **73**, 565 (2001).
- [18] I. Chiorescu, P. Bertet, K. Semba, Y. Nakamura, C. J. P. M. Harmans, and J. E. Mooij, Coherent dynamics of a flux qubit coupled to a harmonic oscillator, *Nature* **431**, 159 (2004).
- [19] A. Wallraff *et al.*, Strong coupling of a single photon to a superconducting qubit using circuit quantum electrodynamics, *Nature* **431**, 162 (2004).
- [20] M. H. Devoret, S. Girvin, and R. Schoelkopf, Circuit-QED: how strong can the coupling between a Josephson junction atom and a transmission line resonator be? *Ann. Phys. (Leipz.)* **16**, 767 (2007).
- [21] T. Niemczyk, F. Deppe, H. Huebl, E. P. Menzel, F. Hocke, M. J. Schwarz, J. J. Garcia-Ripoll, D. Zueco, T. Hümmer, E. Solano, A. Marx, and R. Gross, Circuit quantum electrodynamics in the ultrastrong-coupling regime, *Nat. Phys.* **6**, 772 (2010).
- [22] P. Forn-Díaz, J. Lisenfeld, D. Marcos, J. J. Garcia-Ripoll, E. Solano, C. J. P. M. Harmans, and J. E. Mooij, Observation of the Bloch-Siegert shift in a qubit-oscillator system in the ultrastrong coupling regime, *Phys. Rev. Lett.* **105**, 237001 (2010).
- [23] P. Forn-Díaz, J. J. Garcia-Ripoll, B. Peropadre, J.L. Orgiazzi, M. A. Yurtalan, R. Belyansky, C. M. Wilson, and A. Lupascu, Ultrastrong coupling of a single artificial atom to an electromagnetic continuum in the nonperturbative regime, *Nat. Phys.* **13**, 39 (2017).
- [24] F. Yoshihara, T. Fuse, S. Ashhab, K. Kakuyanagi, S. Saito, and K. Semba, Superconducting qubit-oscillator circuit beyond the ultrastrong-coupling regime, *Nat. Phys.* **13**, 44 (2017).
- [25] F. Yoshihara, T. Fuse, Z. Ao, S. Ashhab, K. Kakuyanagi, S. Saito, T. Aoki, K. Koshino, and K. Semba, Inversion of qubit energy levels in qubit-oscillator circuits in the deep-strong-coupling regime, *Phys. Rev. Lett.* **120** 183601 (2018).
- [26] Z. Chen, Y. Wang, T. Li, L. Tian, Y. Qiu, K. Inomata, F. Yoshihara, S. Han, F. Nori, J. S. Tsai, and J. Q. You, Single-photon-driven high-order sideband transitions in an ultrastrongly coupled circuit-quantum-electrodynamics system, *Phys. Rev. A* **96**, 012325 (2017).
- [27] Shuai-Peng Wang, Guo-Qiang Zhang, Yimin Wang, Zhen Chen, Tiefu Li, J. S. Tsai, Shi-Yao Zhu, and J. Q. You, Photon-Dressed Bloch-Siegert Shift in an Ultrastrongly Coupled Circuit Quantum Electrodynamical System *Phys. Rev. Applied* **13**, 054063 (2020).
- [28] A. F. Kockum, A. Miranowicz, S. D. Liberato, S. Savasta and F. Nori, Ultrastrong coupling between light and matter, *Nat. Rev. Phys.* **1**, 19 (2019).
- [29] P. Forn-Díaz, L. Lamata, E. Rico, J. Kono, and E. Solano, Ultrastrong coupling regimes of light-matter interaction, *Rev. Mod. Phys.* **91**, 025005 (2019).
- [30] D. Zueco, G. M. Reuther, S. Kohler, and P. Hänggi, Qubit-oscillator dynamics in the dispersive regime: Analytical theory beyond the rotating-wave approximation, *Phys. Rev. A* **80**, 033846 (2009).
- [31] S. Ashhab and F. Nori, Qubit-oscillator systems in the ultrastrong-coupling regime and their potential for preparing nonclassical states, *Phys. Rev. A* **81**, 042311 (2010).
- [32] J. Casanova, G. Romero, I. Lizuain, J. J. García-Ripoll, and E. Solano, Deep Strong Coupling Regime of the Jaynes-Cummings Model, *Phys. Rev. Lett.* **105**, 263603 (2010).
- [33] D. Z. Rossatto, C. J. Villas-Bôas, M. Sanz, and E. Solano, Spectral classification of coupling regimes in the quantum Rabi model, *Phys. Rev. A*, **96**, 013849 (2017).
- [34] J. Lolli, A. Baksic, D. Nagy, E. V. Manucharyan, and C. Ciuti, Ancillary Qubit Spectroscopy of Vacua in Cavity and Circuit Quantum Electrodynamics, *Phys. Rev. Lett.* **114**, 183601 (2015).
- [35] L. Garziano *et al.*, Vacuum-induced symmetry breaking in a superconducting quantum circuit, *Phys. Rev. A* **90**, 043817 (2014).
- [36] P. Nataf and C. Ciuti, Vacuum degeneracy of a circuit QED system in the ultrastrong coupling regime, *Phys. Rev. Lett.* **104**, 023601 (2010).
- [37] G. Vacanti, S. Pugnetti, N. Didier, M. Paternostro, G. M. Palma, R. Fazio, and V. Vedral, Photon Production from the Vacuum Close to the Superradiant Transition: Linking the Dynamical Casimir Effect to the Kibble-Zurek Mechanism, *Phys. Rev. Lett.* **108**, 093603 (2012).
- [38] L. Garziano *et al.*, Switching on and off of ultrastrong light-matter interaction: Photon statistics of quantum vacuum radiation, *Phys. Rev. A* **88**, 063829 (2013).
- [39] R. Stassi *et al.*, Spontaneous conversion from virtual to real photons in the ultrastrong-coupling regime, *Phys. Rev. Lett.* **110**, 243601 (2013).
- [40] M. Cirio *et al.*, Amplified optomechanical transduction of virtual radiation pressure, *Phys. Rev. Lett.* **119**, 053601 (2017).
- [41] C. S. Munoz *et al.*, Resolution of superluminal signalling in non-perturbative cavity quantum electrodynamics, *Nat. Commun.* **9**, 1924 (2018).
- [42] J. R. Johansson *et al.*, Dynamical Casimir effect in a superconducting coplanar waveguide, *Phys. Rev. Lett.* **103**, 147003 (2009).
- [43] C. M. Wilson *et al.*, Observation of the dynamical Casimir effect in a superconducting circuit, *Nature* **479**, 376-379 (2011).
- [44] Y. X. Liu *et al.*, Optical Selection Rules and Phase-Dependent Adiabatic State Control in a Superconducting Quantum Circuit, *Phys. Rev. Lett.* **95**, 087001 (2005).
- [45] Sajeev John and Jian Wang, Quantum electrodynamics near a photonic band gap: photon bound states and dressed atoms, *Phys. Rev. Lett.* **64**, 2418-2421 (1990).
- [46] A. Goban *et al.*, Atom-light interactions in photonic crystals. *Nat. Commun.* **5**, 3808 (2014).
- [47] A. Ridolfo *et al.*, Photon Blockade in the Ultrastrong Coupling Regime, *Phys. Rev. Lett.* **109**, 193602 (2012).
- [48] M.-J. Hwang, R. Puebla, and M. B. Plenio, Quantum phase transition and universal dynamics in the Rabi model, *Phys. Rev. Lett.* **115**, 180404 (2015).
- [49] M. Liu, S. Chesi, Z.-J. Ying, X. Chen, H.-G. Luo, and H.-Q. Lin, Universal scaling and critical exponents of the anisotropic quantum Rabi model, *Phys. Rev. Lett.* **119**, 220601 (2017).
- [50] Q.-T. Xie, S. Cui, J.-P. Cao, L. Amico, and H. Fan, Anisotropic Rabi model, *Phys. Rev. X* **4**, 021046 (2014).

Acknowledgments

This work is supported by the National Key Research and Development Program of China (Grant No. 2022YFA1405200), the National Natural Science Foundation of China (Grants No. 92265202, No. 11934010, No. 62074091, and No. U2230402), Tsinghua University Initiative Scientific Research Program. A.R. acknowledges the QuantERA grant SiUCs (Grant No. 731473), the PNRR MUR project PE0000023-NQSTI, and the ICSC C Centro Nazionale di Ricerca in High-Performance Computing, Big Data and Quantum Computing. S.S. acknowledges the Army Research Office (ARO) (Grant No. W911NF1910065). F.N. is supported in part by Nippon Telegraph and Telephone Corporation (NTT) Research, the Japan Science and Technology Agency (JST) [via the Quantum Leap Flagship Program (Q-LEAP), and the Moonshot R&D Grant No. JPMJMS2061], the Asian Office of Aerospace Research and Development (AOARD) (Grant No. FA2386-20-1-

4069), and the Foundational Questions Institute Fund (FQXi) (Grant No. FQXi-IAF19-06). Y.N. was partly supported by the Japan Society for the Promotion of Science (JSPS) Grants-in-Aid for Scientific Research (KAKENHI) (Grant No. 22H04937).

Author contributions

S.W., T.L. and J.Q.Y. conceived the experiment. S.W. performed the experiment. S.W. and A.R. analysed the data. A.R. and S.S. developed the theory. S.W., A.R., T.L., S.S., F.N., Y.N. and J.Q.Y. discussed the results and contributed to the writing of the manuscript.

Competing Interests

The authors declare no competing interest.

Correspondence and requests for materials should be addressed to Tiefu Li, Salvatore Savasta, or J. Q. You.

Supplementary Information for “Probing the symmetry breaking of a light–matter system by an ancillary qubit”

Shuai-Peng Wang,^{1,2} Alessandro Ridolfo,³ Tiefu Li,^{4,5,*} Salvatore Savasta,^{6,†} Franco Nori,^{7,8,9} Y. Nakamura,^{9,10} and J. Q. You^{2,‡}

¹*Quantum Physics and Quantum Information Division, Beijing Computational Science Research Center, Beijing 100193, China*

²*Interdisciplinary Center of Quantum Information, State Key Laboratory of Extreme Photonics and Instrumentation, and Zhejiang Province Key Laboratory of Quantum Technology and Device, School of Physics, Zhejiang University, Hangzhou 310027, China*

³*Dipartimento di Fisica e Astronomia, Università di Catania, 95123 Catania, Italy*

⁴*School of Integrated Circuits, and Frontier Science Center for Quantum Information, Tsinghua University, Beijing 100084, China*

⁵*Beijing Academy of Quantum Information Sciences, Beijing 100193, China*

⁶*Dipartimento di Scienze Matematiche e Informatiche, Scienze Fisiche e Scienze della Terra, Università di Messina, I-98166 Messina, Italy*

⁷*Theoretical Quantum Physics Laboratory, Cluster for Pioneering Research, RIKEN, Wako, Saitama 351-0198, Japan*

⁸*Physics Department, The University of Michigan, Ann Arbor, Michigan 48109-1040, USA*

⁹*RIKEN Center for Quantum Computing (RQC), Wako, Saitama 351-0198, Japan.*

¹⁰*Department of Applied Physics, Graduate School of Engineering, The University of Tokyo, Bunkyo-ku, Tokyo 113-8656, Japan*

ADDITIONAL EXPERIMENTAL DETAILS

The dependency of the resonance frequency of the lumped-element resonator ω_r on the external flux bias $\delta\Phi_{\text{ext}}$ around the optimal point can be approximately described as

$$\omega_r(\delta\Phi_{\text{ext}}) = \frac{\omega_r(0)}{\sqrt{1 + D \cos \theta |\delta\Phi_{\text{ext}}|}}, \quad (1)$$

where the constant $D = -0.18$ and is determined by tuning the fitting curve of ω_{01} in Fig. 2c of the main text when $\omega_r(0)$ is fixed.

Supplementary Fig. 1 shows the the experimental setup.

Supplementary Fig. 2 displays the bare and normalized reflection spectra without the fitting curves of Figs. 2a and 2b in the main text. The abrupt changes in the transmission background around 5.6 GHz and 11.9 GHz can be seen in the bare spectra in Supplementary Figs. 2a and 2b.

Supplementary Fig. 3 displays the calculated excitation spectra ($\omega_{0,n}$) of the total system (the deep-strongly coupled qubit–resonator system plus the Xmon). The observed transitions (ω_{01} , ω_{02} and ω_{03}) in Fig. 2 of the main text correspond to $\omega_{0,1}$, $\omega_{0,3}$ and $\omega_{0,6}$. The sideband transitions in Fig. 2a of the main text correspond to (from inside to outside) $\omega_{4,18} \approx \omega_{04,X} - (\omega_{01} + \omega_{01,X})$, $\omega_{5,20} \approx (\omega_{02} + \omega_{03,X}) - \omega_{02,X}$, $\omega_{5,16} \approx (\omega_{04} + \omega_{01,X}) - \omega_{02,X}$ and $\omega_{5,15} \approx \omega_{05} - \omega_{02,X}$, where $\omega_{n,m} \equiv \omega_{0,m} - \omega_{0,n}$ and $\omega_{0n,X}$ denotes the dressed excitation energy levels of the Xmon. The observation of these high-order sideband transitions near the band edge is a surprise, which may demand a further theoretical study.

THEORY

Theoretical description

We consider a deep-strongly coupled (DSC) system constituted by a flux qubit coupled inductively to a lumped-element resonator through a shared Josephson junction. This system can display a *photonic vacuum symmetry breaking* [1]. Here we demonstrate that the presence of such symmetry breaking can induce the breaking of parity selection rules of an Xmon artificial atom interacting dispersively with the ultrastrongly coupled system via the lumped-element resonator. This selection-rule breaking can then be probed by applying a driving field on the coupled Xmon.

The total Hamiltonian for our three-component system can be written as

$$H_{\text{tot}} = H_s + H_X^{(4)} - g'(a - a^\dagger)(b - b^\dagger), \quad (2)$$

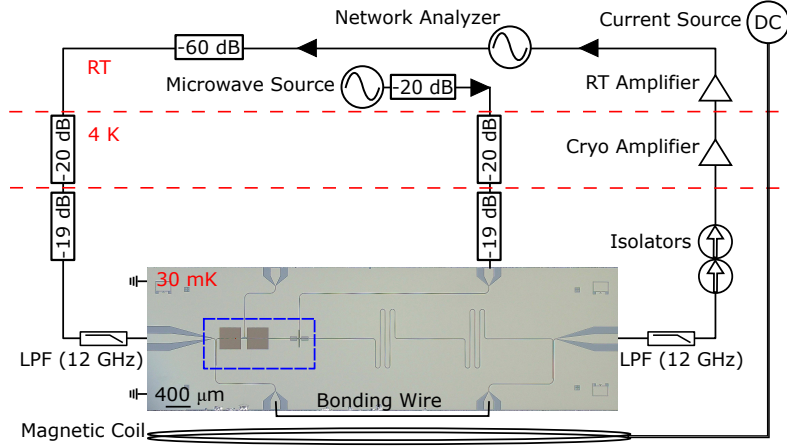
where H_s is the Hamiltonian of the DSC qubit–resonator system in the main text, and

$$b = \sum_{n=0}^3 \sqrt{n+1} |n\rangle \langle n+1| \quad (3)$$

is the annihilation operator for the Xmon modeled here as a four-level artificial atom (qudit). The bare Xmon as a qudit is

$$H_X^{(4)} = \sum_{n=0}^3 \varepsilon_n |n\rangle \langle n|, \quad (4)$$

where we choose $\varepsilon_0 = 0$ for convenience.



Supplementary Fig. 1. Schematic of the experimental setup. Figure 1a in the main text is the area denoted by the blue rectangular box. RT: room temperature. Cryo: cryogenic. LPF: low pass filter.

Owing to the parity symmetry, two-photon transitions in the bare Xmon artificial atom are forbidden. Thus, an observation of the two-photon transition represents a signature of induced breaking of the selection rules in the Xmon coupled to the qubit-resonator system. Below we show that the two-photon transition rate can be directly calculated using second-order perturbation theory.

Let us consider a single-tone external drive exciting the Xmon,

$$H_1(t) = (\Omega/2)(Y^- e^{-i\omega_d t} + Y^+ e^{i\omega_d t}), \quad (5)$$

where

$$Y^+ = -i \sum_{j < k} \langle E_j | (b - b^\dagger) | E_k \rangle | E_j \rangle \langle E_k |, \quad (6)$$

with $|E_j\rangle$ being the eigenstates of the Hamiltonian (2), which are ordered so that $j < k$ if $\omega_j < \omega_k$.

We choose system's ground state $|E_0\rangle$ as the initial state. The first-excited state of the system corresponds to the dressed first-excited state of the DSC qubit-resonator system. The second-excited state of the system corresponds to the dressed first-excited state of the Xmon. The transition rate from $|E_0\rangle$ to $|E_2\rangle$ can be written as

$$W_2(\omega_d) = 2\pi |\mathcal{T}_{0,2}|^2 \delta(\omega_{0,2} - 2\omega_d), \quad (7)$$

where $\omega_{j,k} = \omega_k - \omega_j$, and

$$\mathcal{T}_{0,2} = \sum_k \frac{V_{0,k} V_{k,2}}{\omega_{0,k} - \omega_d}. \quad (8)$$

Here, the matrix elements of the perturbation potential are

$$V_{j,k} = \frac{\Omega}{2} \langle E_j | Y^+ | E_k \rangle. \quad (9)$$

The losses of the system components can be included by converting the Dirac delta function in Supplementary

Eq. (7) into a Lorentzian:

$$\delta(\omega_{0,2} - 2\omega_d) \rightarrow \frac{1}{2\pi} \frac{\Gamma_{0,2}}{(\omega_{0,2} - 2\omega_d)^2 + \Gamma_{0,2}^2/4}. \quad (10)$$

The definition of the loss rates as $\Gamma_{2,0}$ can be found in the next section.

The two-photon Xmon power spectrum can be obtained as

$$\langle Y^- Y^+ \rangle = \text{Tr}[\rho Y^- Y^+], \quad (11)$$

where ρ is system's density operator. It can be written as

$$\langle Y^- Y^+ \rangle = \frac{W_2(\omega_d)}{\Gamma_{0,2}} (|Y_{0,2}|^2 + |Y_{1,2}|^2), \quad (12)$$

where $Y_{j,k} = \langle E_j | Y^+ | E_k \rangle$. In comparison with $Y_{0,2}$, the matrix element $Y_{1,2}$ is almost negligible.

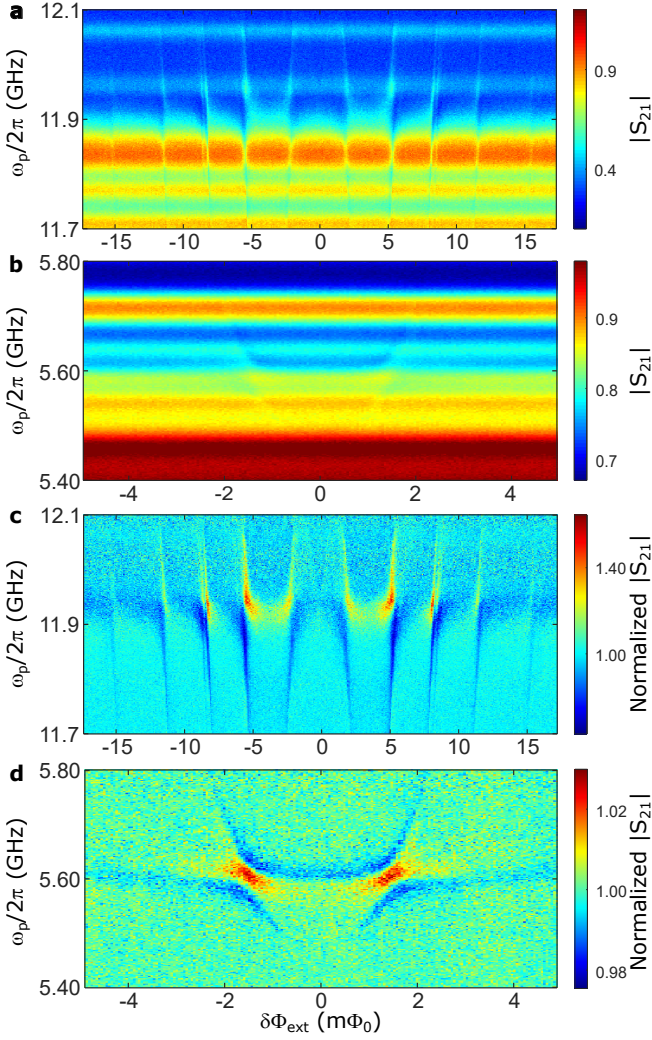
Density matrix approach

Here we derive the two-photon emission rate of the three-component system described in the previous section, by using a perturbative master equation approach. We start from the master equation for the coupled system in the basis of its eigenstates (dressed-states approach), including the external drive (that is the perturbation):

$$\dot{\rho} = i[\rho, H_0 + H_1(t)] + \mathcal{L}[\rho], \quad (13)$$

where $H_0 = \sum_n \omega_n |E_n\rangle \langle E_n|$ is the diagonalized Hamiltonian of Supplementary Eq. (2). The external driving field is described by the time-dependent interaction

$$H_1(t) = \Omega \cos(\omega_d t) (Y^- + Y^+), \quad (14)$$



Supplementary Fig. 2. **a(c)** and **b(d)** are bare (normalized) reflection spectra without the fitting curves of Figs. 2a and 2b in the main text. Source data are provided as a Source Data file.

and $\mathcal{L}[\rho]$ is the dissipator expressed in the eigenstates of the DSC system (see, e.g., Ref. 2). Applying the rotating-wave approximation, we can write

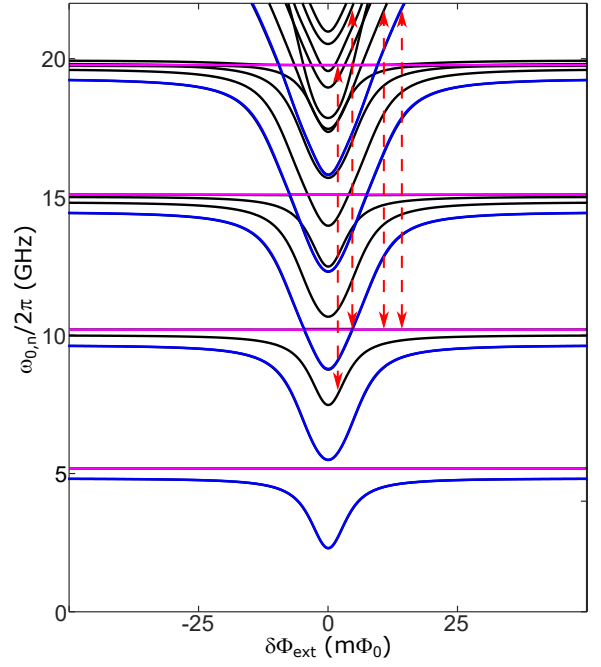
$$H_1(t) = (\Omega/2)(Y^- e^{-i\omega_d t} + Y^+ e^{i\omega_d t}). \quad (15)$$

We will also consider an expansion of the density matrix in terms of powers of the drive amplitude, so that we can separate each contribution, i.e.

$$\rho = \rho^{(0)} + \rho^{(1)} + \rho^{(2)} + \dots = \sum_{n=0}^{\infty} \rho^{(n)}. \quad (16)$$

Moreover, since the drive can be expanded in Fourier components as

$$H_1(t) = \sum_k H_{\omega_k}^{(1)} \exp(i\omega_k t), \quad (17)$$



Supplementary Fig. 3. Calculated excitation spectra of the total system ($\omega_{0,n}$). The parameters used in the calculation are the same as in the main text. The dressed excitation energy levels of the deep-strongly coupled qubit-resonator system ω_{0n} (Xmon $\omega_{0n,X}$) are in blue (magenta). The black levels correspond to multiple excitation levels $\omega_{0n} + \omega_{0m,X}$. The red dashed double-headed lines indicate the observed sideband transitions in Fig. 2a of the main text.

(actually, we will use here only a single-tone drive) the same can be done with $\rho^{(n)}$, leading to the expression

$$\rho = \sum_{n=0}^{\infty} \sum_k \rho_{\omega_k}^{(n)} \exp(i\omega_k t), \quad (18)$$

where $\omega_k = \pm k \omega_d$, with k being an integer number. Considering the steady state, plugging Supplementary Eq. (18) into the master equation, we obtain a set of closed equations separated in driving orders and Fourier components, that at the lowest order looks like:

$$\dot{\rho}^{(0)} = 0 = i[\rho^{(0)}, H_0] + \mathcal{L}[\rho^{(0)}], \quad (19)$$

which leads to the thermal density operator

$$\rho^{(0)} = \frac{1}{\mathcal{Z}} \sum_j \exp\left(-\frac{\hbar\omega_j}{k_B T}\right) |E_j\rangle\langle E_j|, \quad (20)$$

with the partition function $\mathcal{Z} = \sum_j \exp\left(-\frac{\hbar\omega_j}{k_B T}\right)$. The next two sets of equations for the first- and second-order density matrices can be formally derived from the master

equation, and they have the following forms:

$$\begin{aligned}
\dot{\rho}^{(1)}(\omega_k) &= i\omega_k\rho_{\omega_k}^{(1)} \\
&= i[\rho_{\omega_k}^{(0)}, H_{\omega_k}^{(1)}] + i[\rho_{\omega_k}^{(1)}, H_0] \\
&\quad + \mathcal{L}[\rho_{\omega_k}^{(1)}], \\
\dot{\rho}^{(2)}(\omega_j + \omega_k) &= i(\omega_j + \omega_k)\rho_{\omega_j + \omega_k}^{(2)} \\
&= i[\rho_{\omega_j}^{(1)}, H_{\omega_k}^{(1)}] + i[\rho_{\omega_j + \omega_k}^{(2)}, H_0] \\
&\quad + \mathcal{L}[\rho_{\omega_j + \omega_k}^{(2)}]. \tag{21}
\end{aligned}$$

The solutions of the above expressions can be derived sequentially, by plugging the already found solution for the previous order. In this way we find for the first- and second-order steady-state density matrices:

$$\begin{aligned}
(\rho_{\omega_k}^{(1)})_{n,m} &= \frac{(H_{\omega_k}^{(1)})_{n,m}}{\omega_k - \omega_{n,m} + i\Gamma_{n,m}/2} (\rho_{m,m}^{(0)} - \rho_{n,n}^{(0)}), \\
(\rho_{\omega_j + \omega_k}^{(2)})_{n,m} &= \frac{([H_{\omega_j}^{(1)}, \rho_{\omega_k}^{(1)}]_{n,m} + ([H_{\omega_k}^{(1)}, \rho_{\omega_j}^{(1)}]_{n,m})}{\omega_j + \omega_k - \omega_{n,m} + i\Gamma_{n,m}/2}. \tag{22}
\end{aligned}$$

The decay rates $\Gamma_{n,m}$ are the sum of all the lossy channels involved in the $|E_m\rangle \rightarrow |E_n\rangle$ transition and its expression is shown below. For a nonzero temperature reservoir, one has to take care of the modified decay rates for the generic transition $|E_j\rangle \rightarrow |E_i\rangle$ (with $j > i$). For the sake of simplicity, we assume that both the artificial atoms and the lumped-element resonator are thermalized at the same temperature. Thus, the rates can be calculated via the Fermi's golden-rule. At zero-temperature, we obtain $\Gamma_{i,j}^0 = \gamma_{i,j}^{(q)} + \gamma_{i,j}^{(a)} + \gamma_{i,j}^{(b)}$, where $\gamma_{i,j}^{(q)} = \gamma_q |\langle E_i | \sigma_x | E_j \rangle|^2$, $\gamma_{i,j}^{(a)} = \gamma_a |\langle E_i | (a + a^\dagger) | E_j \rangle|^2$, and $\gamma_{i,j}^{(b)} = \gamma_b |\langle E_i | (b + b^\dagger) | E_j \rangle|^2$. At $T > 0$, the loss rates become

$$\Gamma_{i,j} = \sum_{s=\{q,a,b\}} \left(\sum_{k>i} \gamma_{i,k}^{(s)} (1 + 2\bar{n}_{i,k}) + \sum_{k>j} \gamma_{j,k}^{(s)} (1 + 2\bar{n}_{j,k}) \right), \tag{23}$$

where $\bar{n}_{i,j}$ is the thermal noise that affects the $|E_j\rangle \rightarrow |E_i\rangle$ transition, i.e., $\bar{n}_{i,j} = 1/[\exp(\hbar\omega_{i,j}/k_B T) - 1]$. In the following theoretical analysis, corroborated by the standard working temperature of the DSC system ($T \sim 30$ mK), we can safely ignore the enhancement induced rates, by choosing the relevant $\bar{n}_{i,j} = 0$.

In our calculations, we stop the perturbative development up to the second order, as the essential physics is fully caught. In particular, we can obtain the single- and two-photon absorption by looking at the polarization of the Xmon as a function of the drive frequency, which can be defined as $\langle P(\omega_d) \rangle = \text{Tr}[-i(b - b^\dagger)\rho(\omega_d)]$. In this formula, we can apply further simplifications by (i) considering the case of a ground state environment ($T = 0$) and (ii) dropping the negligible terms of $\langle P(\omega_d) \rangle$, finding that the leading terms that drive the onset of the sought

effect yield

$$|\langle P(\omega_d) \rangle| \simeq |(Y_{2,0}\rho_{0,2}^{(2)} + Y_{0,2}\rho_{2,0}^{(2)})| = 2\Re[Y_{2,0}\rho_{0,2}^{(2)}]. \tag{24}$$

Terms like $Y_{2,0}\rho_{0,2}^{(1)} + Y_{0,2}\rho_{2,0}^{(1)}$ represent a constant background as they are far-detuned resonances, and thus they can be ignored. Furthermore, we also find that $|Y_{2,0}| \simeq 1$, as it represents the transition matrix element of the weakly coupled Xmon, from its ground to the first-excited level. Following our perturbative approach, we find that

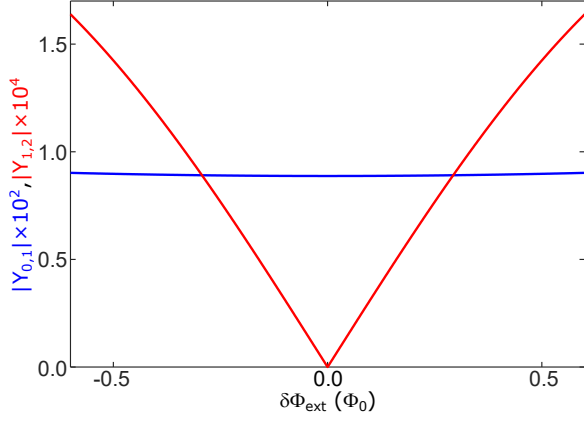
$$\rho_{0,2}^{(2)} = -\frac{\Omega^2}{2} \frac{Y_{0,1}Y_{1,2}}{(\omega_d - \omega_{0,1} + i\Gamma_{0,1}/2)(2\omega_d - \omega_{0,2} + i\Gamma_{0,2}/2)}. \tag{25}$$

Finally, as the detected field has frequency $\omega_d \sim \frac{1}{2}\omega_{2,0}$, the non-resonant part of the denominator can be expanded in series, leading to the final expression:

$$|\langle P(\omega_d) \rangle| = \frac{\Omega^2 |Y_{0,1}Y_{1,2}|}{\omega_{1,2} - \omega_{0,1}} \frac{\Gamma_{0,2} |Y_{2,0}|}{(2\omega_d - \omega_{0,2})^2 + \Gamma_{0,2}^2/4}. \tag{26}$$

Results

Below we show the numerical results achieved with parameters extrapolated by the experimental data. Namely, we use $\omega_r/2\pi = 4.82$ GHz, $\Delta/2\pi = 15$ GHz, $g/2\pi = 4.55$ GHz, $g'/2\pi \approx g_X/2\pi = 28$ MHz, and loss rates for the flux qubit, lumped-element resonator and Xmon are chosen to be $\gamma^{(q)}/2\pi = \gamma^{(a)}/2\pi = \gamma^{(b)}/2\pi = 2$ MHz. Also, we consider a thermalized DSC system at a temperature of 30 mK. Our model is able to reproduce the experimental results with a very good agreement. In the simulations, we use a quite strong external field exciting the Xmon, in order to produce a two-photon absorption, and its value in terms of linewidth is $\Omega = 200 \times \gamma^{(b)}$.

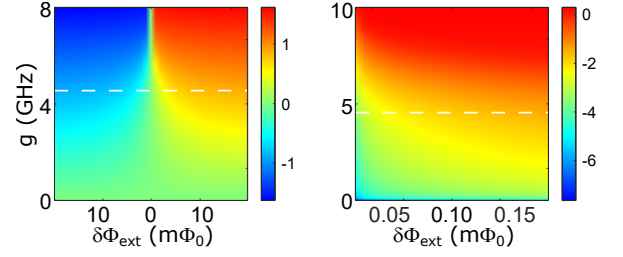


Supplementary Fig. 4. Calculated most relevant terms in the two-photon absorption rate as a function of the external flux bias $\delta\Phi_{\text{ext}}$. The detected signal is approximately proportional to the product of these quantities. The calculated $Y_{1,2}$ term goes to zero for $\delta\Phi_{\text{ext}} \rightarrow 0$, when the parity selection rule for the dressed Xmon is restored. The $Y_{0,2}$ is not shown in the figure as it is almost unity in the whole range investigated here.

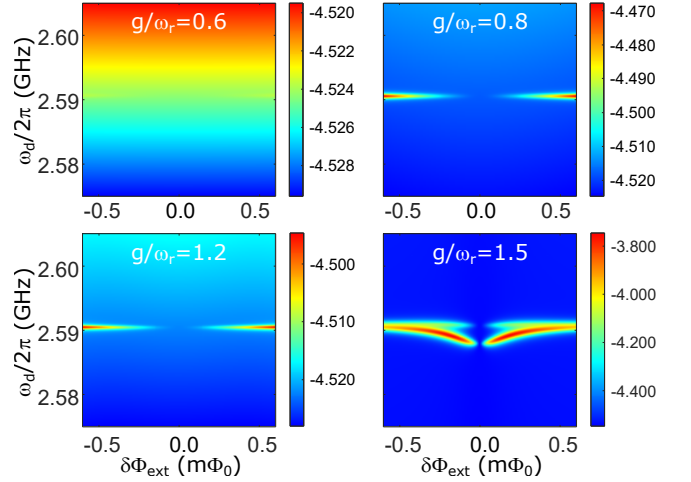
Such a value is large enough to ensure the onset of the second-order processes. While for the direct excitation of the single-photon absorption, we reduce Ω by a factor 2×10^6 , in doing so we can get the same order of the amplitudes of the single- and two-photon signals, which is consistent with the experimental observation.

Figure 3 in the main text shows the comparison between experimental (top) and theoretical (middle) results calculated for the reported parameters. The left panel shows the weak-excitation, two-tone spectroscopy of the dressed Xmon ($|E_0\rangle \rightarrow |E_2\rangle$) transition, while in the right panel, a strong-excitation spectroscopy shows the two-photon resonance at half of the Xmon ($|E_0\rangle \rightarrow |E_2\rangle$) transition. Both the experimental and theoretical signals are displayed as a function of the drive frequency ω_d and of the external flux bias, $\delta\Phi_{\text{ext}}$. For zero flux bias $\delta\Phi_{\text{ext}} = 0$, the two-photon resonance disappears as the parity symmetry is completely restored. The theoretical calculations display the changes in the amplitude of the Xmon polarization $|\langle P(\omega_d) \rangle|$.

Supplementary Fig 4 displays the most relevant term in the two-photon absorption rate as a function of the flux bias $\delta\Phi_{\text{ext}}$. It shows the origin of the dependence on the flux bias of the two-photon transition rate for the dressed Xmon. In particular, we observe that the matrix element $Y_{1,2}$ goes to zero for $\delta\Phi_{\text{ext}} \rightarrow 0$, owing to the restoration of parity symmetry. This disables two-photon transitions from the ground state to the dressed first excited state of the Xmon ($|E_0\rangle \rightarrow |E_2\rangle$).



Supplementary Fig. 5. Calculated ground-state coherence $\langle G|a|G \rangle$ of the qubit–resonator system. Left: ground-state coherence $\langle G|a|G \rangle$ versus both the external flux bias $\delta\Phi_{\text{ext}}$ and the coupling strength g . The dashed white line represents the measured value of coupling strength in the experiment. Right: as in the left figure, the ground-state coherence $\langle G|a|G \rangle$ is shown only for positive flux bias, and for higher values of the coupling. The scale of the right figure is logarithmic, with a small cutoff to the zero flux bias in order to avoid the log-divergence.



Supplementary Fig. 6. Simulated two-photon spectra of the Xmon versus the effective coupling strength g/ω_r . The negative value of the plot legend is due to the log-scale. The drive intensity applied is the same as in Fig. 3d in the main text.

Further discussions

Supplementary Fig. 5 displays the calculated ground-state coherence $\langle G|a|G \rangle$ of the qubit–resonator system versus both the external flux bias $\delta\Phi_{\text{ext}}$ and the coupling strength g . The vacuum expectation value $\langle G|a|G \rangle$ becomes non-negligible when the coupling strength g approaches deep strong and the external flux bias $\delta\Phi_{\text{ext}}$ is tuned away from the optimal point.

Supplementary Fig. 6 displays the simulated results of the two-photon spectra of the Xmon versus the effective coupling strength g/ω_r . We can see that when the effective coupling strength g/ω_r is reduced to 0.6, the two-photon signals of the Xmon disappear. For stronger coupling ($g/\omega_r = 1.5$), further features emerge due to

the interaction of the two-photon resonance with other spectral lines.

Symmetry breaking of the quantum vacuum makes the flux-bias-insensitive Xmon experience a *virtual* path to its two-photon resonance. It is not possible if the Xmon is coupled with a normal product-state vacuum (when $g/\omega_r \ll 1$), or when the vacuum symmetry is preserved ($\delta\Phi_{\text{ext}} = 0$), in contrast to the cases of flux-tunable qubits, where the two-photon transition becomes allowed naturally when there is a finite external flux bias.

[†] salvatore.savasta@unime.it

[‡] jqyou@zju.edu.cn

- [1] L. Garziano, R. Stassi, A. Ridolfo, O. Di Stefano, and S. Savasta, Vacuum-induced symmetry breaking in a superconducting quantum circuit, *Phys. Rev. A* **90**, 043817 (2014).
- [2] A. Ridolfo, M. Leib, S. Savasta, and M. J. Hartmann, Photon Blockade in the Ultrastrong Coupling Regime, *Phys. Rev. Lett.* **109**, 193602 (2012).

* lif@tsinghua.edu.cn